Subtidal circulation in a deep-silled fjord: Douglas Channel, British Columbia

Di Wan, Charles G. Hannah, Michael G.G. Foreman, and Stan Dosso

May 2017

AGU PUBLICATIONS

JGR

Journal of Geophysical Research: Oceans

RESEARCH ARTICLE

10.1002/2016JC012022

Subtidal circulation in a deep-silled fjord: Douglas Channel, British Columbia

Di Wan[1,2], Charles G. Hannah[2], Michael G. G. Foreman[2], and Stan Dosso[1]

[1]School of Earth and Ocean Sciences, University of Victoria, Victoria, BC, Canada, [2]Institute of Ocean Sciences, Department of Fisheries and Oceans, Sidney, BC, Canada

Key Points:
- An annual 3 month long deep water renewal replenishes the deep basin water in Douglas Channel
- The observed landward net volume flux suggests the importance of the complex channel network to the system
- Counter-wind current velocity response is observed at 100–120 m depth

Supporting Information:
- Supporting Information S1

Correspondence to:
D. Wan,
diwan@uvic.ca

Citation:
Wan, D., C. G. Hannah, M. G. G. Foreman, and S. Dosso (2017), Subtidal circulation in a deep-silled fjord: Douglas Channel, British Columbia, *J. Geophys. Res. Oceans*, *122*, 4163–4182, doi:10.1002/2016JC012022.

Received 2 JUN 2016
Accepted 12 FEB 2017
Accepted article online 15 FEB 2017
Published online 22 MAY 2017

Abstract Douglas Channel, a deep fjord on the west coast of British Columbia, Canada, is the main waterway in the fjord system that connects the town of Kitimat to Queen Charlotte Sound and Hecate Strait. A 200 m depth sill divides Douglas Channel into an outer and an inner basin. This study examines the low-frequency (from seasonal to meteorological bands) circulation in Douglas Channel from data collected at three moorings deployed during 2013–2015. The deep flows are dominated by a yearly renewal that takes place from May/June to early September. A dense bottom layer with a thickness of 100 m that cascades through the system at the speed of 0.1–0.2 m s^{-1}, which is consistent with gravity currents. Estuarine flow dominates the circulation above the sill depth, and the observed landward net volume flux suggests that it is necessary to include the entire complex channel network to fully understand the estuarine circulation in the system. The influence of the wind forcing on the subtidal circulation is not only at the surface, but also at middepth. The along-channel wind dominates the surface current velocity fluctuations and the sea level response to the wind produces a velocity signal at 100–120 m in the counter-wind direction. Overall, the circulation in the seasonal and the meteorological bands is a mix of estuarine flow, direct wind-driven flow, and the barotropic and baroclinic responses to changes to the surface pressure gradient caused by the wind stress.

1. Introduction

The north coast of British Columbia is a complex network of islands, waterways, mountains, and deep fjords (Figure 1). This area is at the core of the region called the Great Bear Rainforest [*Young et al*., 1997] which has been the subject of extensive planning to reduce land use conflicts [*Saarikoski et al*., 2013; *Government of British Columbia*, 2016]. Increased marine activity, including proposals for the transport of diluted bitumen and liquefied natural gas (LNG) from terminals in Kitimat BC, requires an improved understanding of the physical oceanography of the region to support oil response planning and to provide enhanced information for navigation. In addition, there is an increasing need for oceanographic information to support both conservation goals and the management of the marine resources.

The oceanography of the adjacent continental shelf was studied extensively from 1982 to 1995 (*Crawford* [2001] contains an extensive bibliography and much of the data) but there has been much less work done in the inlets and fjords. The first systematic observational program was George Pickard's pioneering fjord work in the 1950s [*Pickard*, 1961]. During 1977 and 1978 extensive measurements were made in Douglas Channel in relation to a large hydropower project [*Webster*, 1980a,1980b; *Macdonald*, 1983]. These studies provide basic descriptions of the water properties, the estuarine nature of the surface flows, and the importance of the wind forcing on the surface currents. Douglas Channel can be classified as a partially mixed estuary by the classification given by *Hansen and Rattray* [1966], having a smooth density transition between the freshwater layer and the bottom. There was also the indication of a summertime renewal of the deep water. *Webster* [1980b] and *Macdonald et al*. [1983] concluded a complete replenish of the basin water based on the changes in T/S graphs between July and September. However, due to instrument limitations at the time, these early studies were unable to describe the circulation structure of the entire water column or to provide a definitive description of the deep basin water exchange, but they motivate us to quantitatively describe the circulation, including the renewal event in the deep basin.

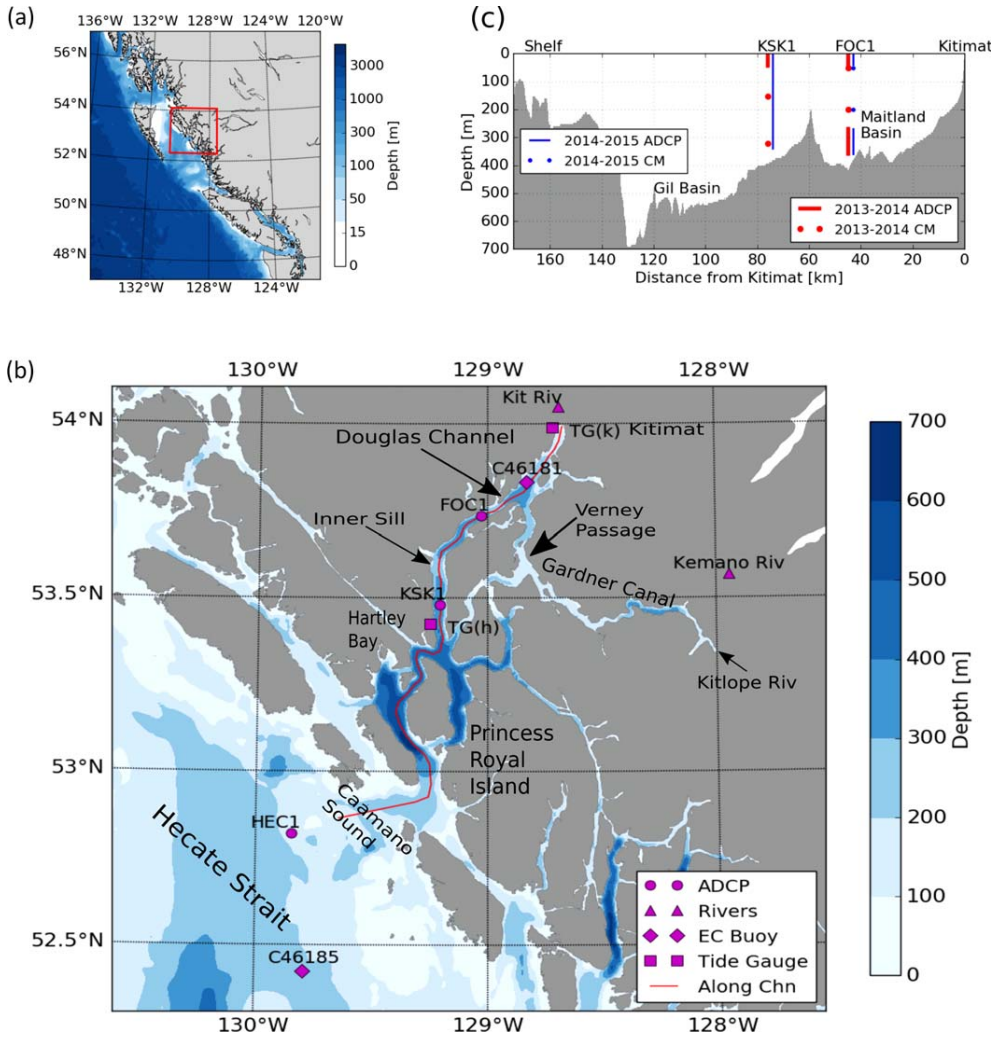

Figure 1. (a) Bathymetry of the west coast Canada. The Kitimat system is the region marked with the red square that is zoomed in Figure 1b Kitimat system bathymetry and locations of observation stations. Mooring stations (round circles), river gauges (triangles), Environment Canada Buoys (diamonds), and tide gauge locations (squares) are marked on the map. The bathymetry along the red along-channel route is shown in Figure 1c, along with the two mooring locations and the current velocity data availability during two deployments (ADCP denotes Acoustic Doppler Current Profiler; CM denotes single point current meter).

The focus of this paper is Douglas Channel, the component of the main navigation channel which extends from Kitimat to Gil Basin (just beyond Hartley Bay), a distance of about 90 km (Figure 1). A comprehensive description of the region is provided by *Macdonald* [1983]; here we summarize some relevant details. Douglas Channel is one component of the fjord system that connects the inland waters with Hecate Strait via long, narrow and deep channels. The distance from the mouth of the Kitimat River to Hecate Strait is about 140 km. An important feature of the system is that the fjord sills are relatively deep. The extended sill where the fjord system connects with Hecate Strait is about 140 m deep, and the inner sill is about 200 m deep. With the focus on Douglas Channel, the inner sill between the mooring locations at FOC1 and KSK1 is of particular interest here; it is about 200 m deep in the middle of the channel and 220 m deep on the sides (Figure 1b). This sill separates the basins into an inner basin (Maitland Basin, landward) and an outer basin (Gil Basin, seaward). Shallow silled fjords such as Knight Inlet (60 m sills), an extensively studied fjord at the southern end of the Great Bear Rainforest [*Farmer and Smith*, 1980; *Baker and Pond*, 1995], are useful but imperfect analogues for Douglas Channel. For the subtidal circulation in Douglas Channel, we expect estuarine flows in the upper layers, relatively quiet deep basin water, and wind-driven circulation at the surface; however, different renewal processes are expected in the deep water because of the relatively deep sill.

Table 1. CTD Depths at Three Moorings[a]

Station	Deployment	CTD Depth (m)
FOC1	2013–2014	16, 53, 150, 317, 353
	2014–2015	12, 36, 50, 146, 298, 354
KSK1	2013–2014	19, 154, 323
	2014–2015	15, 40,150, 362
HEC1	2013–2014	61, 133
	2014–2015	18, 42, 55, 132*

[a]The CTD at 132 m at HEC1 failed on 28 November 2014.

2. Data Description

2.1. Data Inventory

Three moorings (FOC1, KSK1, and HEC1 in Figure 1c) were deployed from July 2013 to July 2014 and again from July 2014 to July 2015. FOC1 is located inside of the inner sill of Douglas Channel and KSK1 is located outside of the inner sill (Figure 1b). The most complete observations were obtained during the second deployment (2014–2015); therefore, we focus the velocity analyses on this second deployment. At FOC1, there is an upward looking ADCP at 39 m (300 kHz, 4 m bin size), single point current meters at 53 and 200 m, a downward looking ADCP at 100 m above the bottom (300 kHz, 4 m bin size). At KSK1, there is an upward looking ADCP at 40 m (300 kHz, 2 m bin size) and at 11 m from the bottom (75 kHz, 16 m bin size), and a single point current meters at 150 m. The detailed mooring configuration can be found in *Wright et al.* [2016].

Continuous CTD (Conductivity, Temperature, and Depth) data were collected at various depths at these three moorings (Table 1). Ship-based CTD profiles (July 2013, April 2014, July 2014, and September 2014) were also collected throughout the fjord system [*Wright et al.*, 2015, 2016]. The moored CTDs were calibrated before and after each deployment against the ship-based CTD, and the ship-based CTD was calibrated regularly by the manufacturer, and against the water samples collected on multiple stations during each cruise. All salinity values in this paper are given on the Absolute Salinity scale.

Concurrent data that were also analyzed include sea surface elevation data [obtained from Canadian Hydrographic Service websites: http://www.meds-sdmm.dfo-mpo.gc.ca/isdm-gdsi/twl-mne/index-eng.htm at Kitimat (Station 9140) and Hartley Bay (Station 9130), labeled as TG(k) and TG(h), respectively, in Figure 1b]; wind data (taken from Environment Canada Buoys (C46181 and C46185 in Figure 1c); and river discharge and the precipitation records (Environment Canada Wateroffice https://wateroffice.ec.gc.ca/google_map/google_map_e.html?searchBy=p&province=BC). The sea surface elevation observations were corrected to an equipotential gravitational surface using the Canadian Geodetic Vertical Datum (CGVD2013) with an uncertainty as large as 5 cm (B. de Lange Boom, personal communication), and averaged over 5 min intervals to reduce high frequency noise before applying any further processing.

2.2. Data Processing

The sampling frequency of the observational data varied from 1 min (e.g., sea surface elevation data) to 1 h, except for the bottom CTD at FOC1, where sampling interval was 3 h during both deployments. The occasional missing data were filled by linear interpolation. All data were then low-pass filtered to remove the high frequency signal as described below, and resampled at hourly intervals to maintain consistency with the original data.

To remove tidal currents, the *Godin* [1972] filter was applied as a low-pass filter, with the hourly data smoothed twice using a 24 h running average and once using a 25 h running average. This filter effectively removes all the diurnal and semidiurnal signals, but with slight leakage in the O_1 band. While the relatively slow transition at the stop-band also leads to attenuation in the range of 2–3 days [*Thomson and Emery*, 2014], this simple low-pass filter is sufficient for the purpose of this paper. Unless otherwise specified, for the purpose of consistency, all data (including winds) described hereafter were low-passed with the Godin filter.

The width of Douglas Channel does not exceed 5 km and the first internal Rossby radius is about 8 km, thus we expect the cross-channel currents to be small. In addition, Douglas Channel has steep sides typical of fjords, so the wind direction is mostly confined along the channel (the cross-channel wind velocity is one order of magnitude smaller than the along-channel velocity). In this paper, we resolve the ocean currents and the wind velocities into the along-channel and cross-channel components, and focus on the along-channel component.

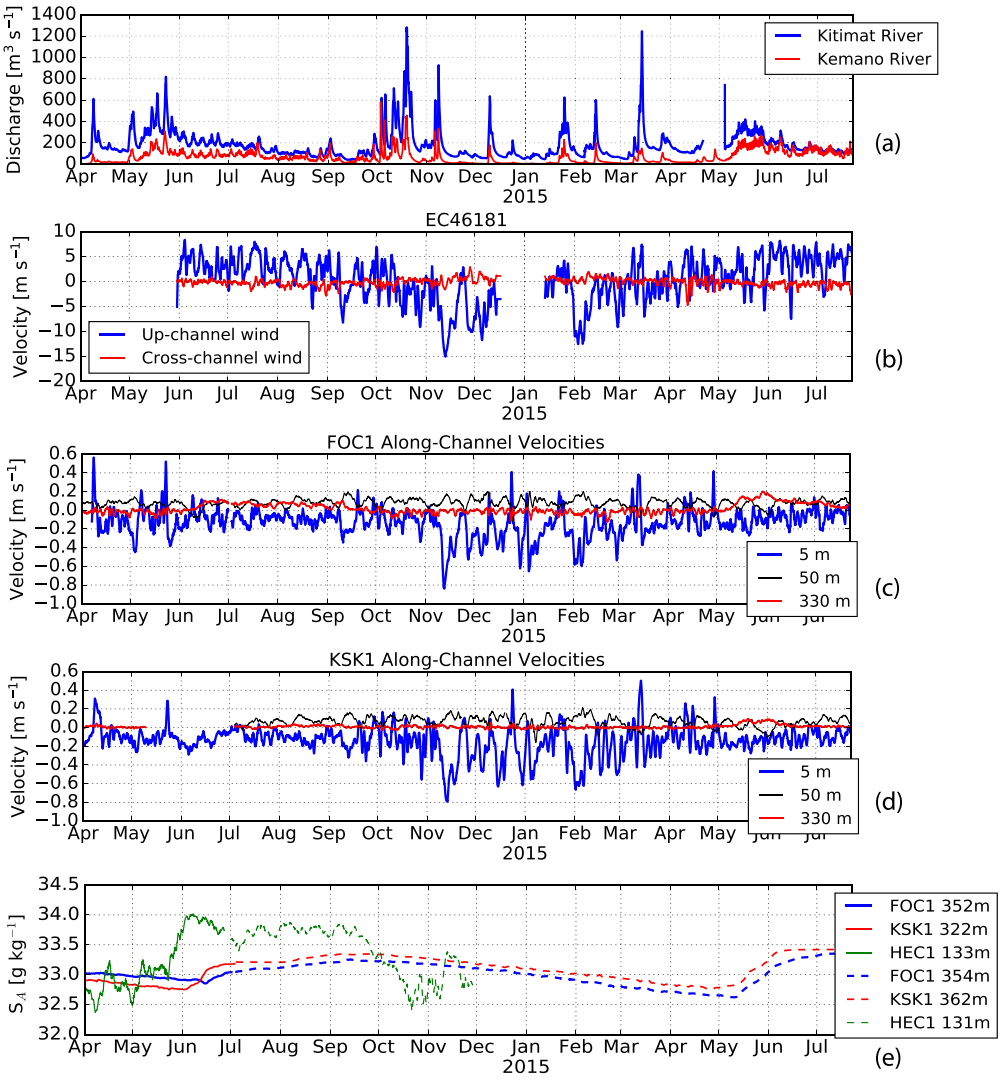

Figure 2. Time series (positive velocity points to up-fjord) of (a) the hourly Kitimat and Kemano River discharge, (b) the low-passed wind velocity measured at EC46181, (c and d) the low-passed surface, middepth, and the bottom current velocities at KSK1 and FOC1, respectively, and (e) the bottom Absolute Salinity at three mooring stations. Supporting information Figures S2 and S3 show the zoomed in version during the renewal seasons in 2014 and 2015, respectively.

3. Seasonal Circulation

3.1. Data Overview

First, we present an overview of the observational data (Figure 2) analysis before further analyses and discussions. As discussed above, we generally focus on the data collected during the second deployment (2014–2015), which provide better velocity coverage at KSK1. For the along-channel velocities, the up-fjord direction as defined as positive.

The freshwater input into the system comes from two sources: snow melt and rain. The time series of Kitimat River discharge (Figure 2a) shows that discharge due to snow melting tends to start in spring (May) and end in late summer (August), whereas discharge due to rain tends to be sporadic, and cause large and sudden discharges during winter seasons (October–March). The annual average rainfall at Kitimat (Station 08FF001) is 2.5 m per year and 4.5 m at Hartley Bay (Station 08FE003) (Environment Canada websites: https://wateroffice.ec.gc.ca/report/). On a cruise to the area one of the authors commented that the water seems to leap off the mountains into ocean when it rains. The very substantial local rainfall means that local run off is an important source of freshwater for the channel.

Given that only two rivers in the region are gauged (the Kitimat and Kemano Rivers, Figure 1), other methods must be used to estimate the total freshwater flux into Douglas Channel and Gardner Canal. Using watershed areas, *Webster* [1980b] estimated that the freshwater flux into Douglas Channel was three times the Kitimat River flow and the flux into Gardner Canal was 17 times the Kemano River flow. Given mean annual fluxes of 150 $m^3\ s^{-1}$ for the Kitimat River and 45 $m^3\ s^{-1}$ for the Kemano River (averages for the period 1970–2010, Environment Canada) this yields a mean freshwater input of 1215 $m^3\ s^{-1}$ (38 km^3 per year). On the other hand, using a simplified watershed model, *Morrison et al*. [2012] estimated the freshwater fluxes for all the major watersheds basins in British Columbia. Consideration of the individual watersheds in the Caamaño region shows that the total annual freshwater flux into Douglas Channel and Gardner Canal is 1270 $m^3\ s^{-1}$ (40 km^3 per year) with 40% into Douglas Channel and 60% into Gardner Canal (P. Thupaki and J. Morrison, personal communication, 2016). Their results also showed that the interannual variability was about 10% of the mean. Thus the two estimates are consistent.

The only weather buoy (EC46181) located in the channel is between Station FOC1 and Kitimat (Figure 1). From April to August, the average wind direction is up-fjord and the magnitude is smaller than 7 m s^{-1}. Starting from September to October, the mean wind shifts to down-fjord easterly winds (Figure 2b). Episodes of strong down-fjord winds (10–15 m s^{-1}) can last for a few days (e.g., February 2015). On occasion, the anemometer sensor may freeze during winter. For example, during our deployments, the anemometer stopped working from early February to May 2014 and again from mid-December 2014 to early January 2015.

Surface, middepth and the bottom low-passed velocities at FOC1 and KSK1 are shown in Figures 2c and 2d. The variation in the surface (5 m) current velocities at both FOC1 and KSK1 is clearly connected with the along-channel wind, and we discuss this connection in detail in the next section. The velocities at the surface and the middepth (at 50–100 m) suggest a persistent estuarine circulation pattern, such that the surface velocities are in the down-fjord direction and the middepth velocities are generally in the up-fjord direction. The velocities at the bottom in both basins are smaller than near the surface but are not negligible. In summer (May–September) they are typically about 10 cm/s; in winter, they are around 3–5 cm/s. A closer examination shows that the bottom water undergoes a renewal cycle that lasts for 3–4 months in summer as indicated by the changes of the salinity (June–September in Figure 2e). This renewal signal is also accompanied by an up-channel bottom velocity as shown in Figures 3b and 4b. The bottom salinity increases rapidly over 2 weeks in 2014 (the first 2 weeks of June for KSK1, and the last 2 weeks of June for FOC1), and over 4 weeks in 2015 (both KSK1 and FOC1); the salinity then gradually increases throughout the summer in 2014 until September (Figure 2e). Unfortunately, the bottom CTD at HEC1 on the shelf failed at the end of November 2014, but from the bottom salinity measured during the first deployment (2013–2014, shown in Figure 2e, solid lines), we can see that the increase of the basin water salinity follows a rapid increase of the shelf bottom salinity (HEC1), and this increases stops at the end of September when the shelf bottom salinity starts to slowly decline until the next renewal event.

The deep density increase at HEC1 is likely caused by the regional transition from the downwelling to upwelling favourable winds in May/June [*Thomson*, 1981], and this condition lasts until August–September. This seasonal transition in the wind can also be seen from the wind time series inside Douglas Channel. From September to mid-October 2014, the wind transitions from up-fjord direction to down-fjord direction, and it transitions back around May 2015.

Not only does the renewal inflow affect the bottom basin flow patterns, it also affects the vertical structure of the currents. Looking at the velocity profiles (Figures 3 and 4), we see an inflow of bottom water extending from about 150 m to the bottom at both KSK1 and FOC1 stations from May to mid-September. The roughly 50 m thick outflowing layer at 180–230 m depth at KSK1 from November 2014 to March 2015 in Figure 4b is lifted by the bottom renewal layer to about 100–150 m depth during renewal periods with transition periods in between. The surface 40 m profile also reflects this seasonal difference. At KSK1 (Figure 4a), the outflowing surface layer is about 30 m thick in summer (May–September), and thinner but highly variable in winter (October to April). The timing of the renewal event is generally consistent with the timing of upwelling to downwelling to upwelling transitions [*Thomson*, 1981], the wind patterns inside of Douglas Channel (Figure 2b) and the salinity patterns at HEC1 (Figure 2e). We therefore divide the time series into two different seasons: the summer renewal season (from early May to mid-September) and the winter season (mid-September to early May).

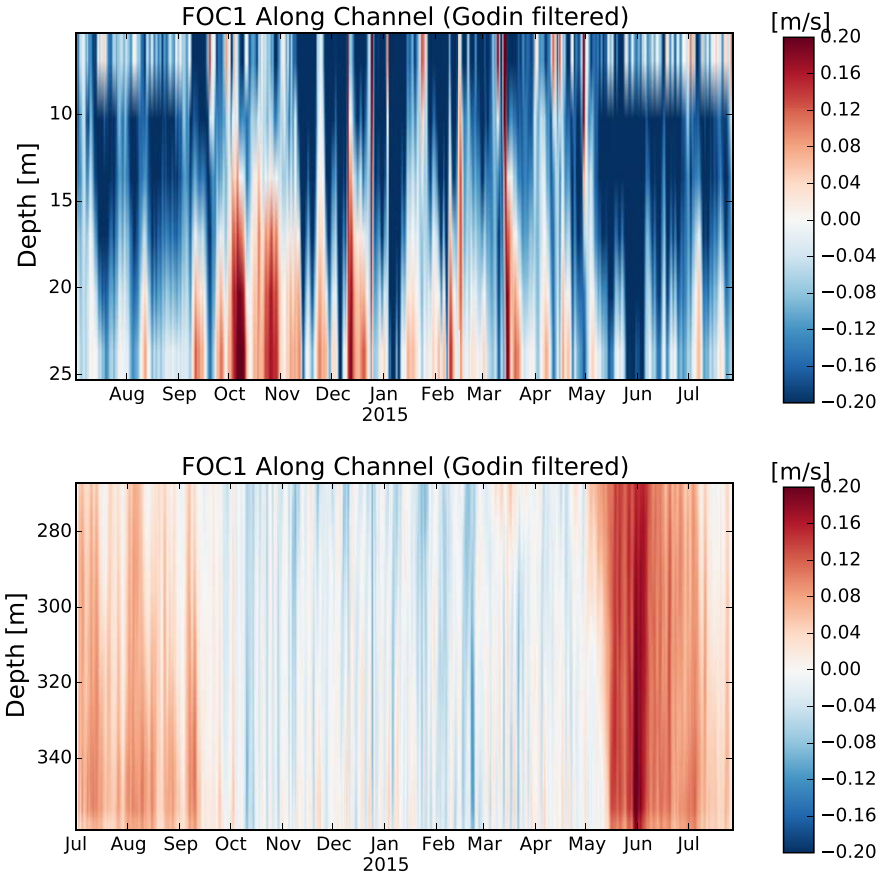

Figure 3. Low-passed ADCP velocity time series for the period 3 July 2014 to 22 July 2015 from mooring FOC1: (top) the upward looking ADCP at 38 m depth, and (bottom) the downward looking ADCP at 260 m depth. The red color (positive) represents the in-fjord direction velocity, and the blue color (negative) represents the down-fjord direction velocity.

3.2. Velocity Profile

The most striking feature of the velocity profiles is the difference in the layer structure between summer and winter (Figure 5) with four layers present in summer and three in winter. The layer structure is common between stations FOC1 and KSK1. In both seasons, the upper two layers are estuarine-like with surface outflow and inflow immediately below. Seasonal changes occur in the lower water column. The summer data show the deep inflow of the renewal water with a compensating outflow layer above, whereas the winter shows a weak outflow. At the surface the average up-fjord winds in the summer ($\approx$ 3 m s^{-1}) reduce the surface velocities; the effect is more pronounced at FOC1 than KSK1. The features of the seasonal velocity structure are also evident in the 2013–2014 data at FOC1 and KSK1 (supporting information Figure S4 and S5). The data coverage at KSK1 in 2013–2014 did not allow for a full water column analysis, but the structure in the upper 50 m is consistent with that shown here. In Figure 5, the time periods for the summer averaging are 2 July to 10 September 2014 and 11 May to 22 July 2015, while the time period for the winter averaging is 11 September 2014 to 10 May 2015. For both stations, there were no reliable measurements of velocity at depths shallower than 5 m or deeper than 360 m, due to the mooring configurations.

In the spline fits, the curves were interpolated and extrapolated from 0 to 360 m to illustrate the velocity layer structure and for the layer transport calculations. Given that the depths at these two stations are about 380 m, this treatment means we do not take the bottom 20 m into account, although we do not expect large velocities there. The top 5 m velocities are extrapolated from the observations, but the contribution of the top 5 m to the mean profile is less than 0.001 m s^{-1} so this extrapolation is not a big contributor to the net flux that is analyzed later.

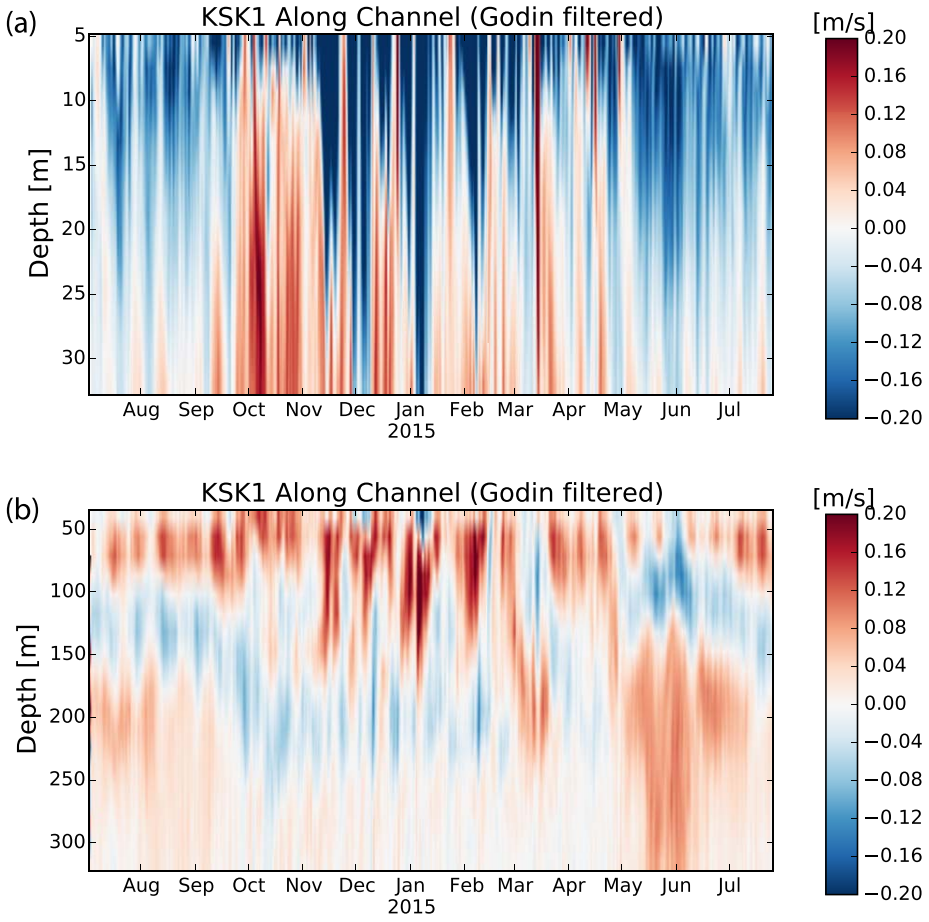

Figure 4. Low-passed ADCP velocity time series for the period 2 July 2014 to 22 July 2015 from mooring KSK1: (top) the upward looking ADCP at 39 m depth, and (bottom) the upward looking ADCP at 360 m depth. The red color (positive) represents the in-fjord direction velocity, and the blue color (negative) represents the down-fjord direction velocity.

There are detailed differences in the vertical structures of the deep flows at KSK1 and FOC1. The deep winter outflow at KSK1 is concentrated in a 80 m thick layer centered at about 200 m depth, whereas the deep outflow at FOC1 covers most of the water column from 150 m to the bottom. Because not all the outflow deep water from the inner basin (FOC1) can make it over the sill to the outer basin (KSK1), and the water that does make it is not dense enough to sink to the bottom of the outer basin, an elevated and thinner outflow at KSK1 (centered at 200 m) is present. Similar flow features have also been observed in the Strait of Georgia by *Masson and Cummins* [2007]. The deeper summer inflow at KSK1 is also centered at about 200 m depth whereas at FOC1 the inflow covers the lower layer from 250 m to the bottom and is bottom intensified (in 2013–2014 it was more vertically uniform over the lower 100 m). These differences suggest that the 200 m deep sill between KSK1 and FOC1 has the biggest impact on the bottom inflow water in the inner basin (renewal season), and on the outflow at the sill depth in the outer basin (winter).

3.3. Deep Water Renewal

In fjords, yearly renewals are usually associated with the appearance of the dense water at the mouth of the fjord [*Syvitski et al.*, 1987]. In early summer (May to June), dense water becomes available at HEC1 (Figure 6) and starts to fill both the inner and the outer basins. From May/June to mid-September, there is a continuous renewal in the outer basin in the layer extending from 150 m to the bottom, "lifting" the overlaying layers up. As shown in Figure 5, the zero velocity crossing for the bottom of the second layer at KSK1 is displaced upward from 150 m in winter to 80 m in summer.

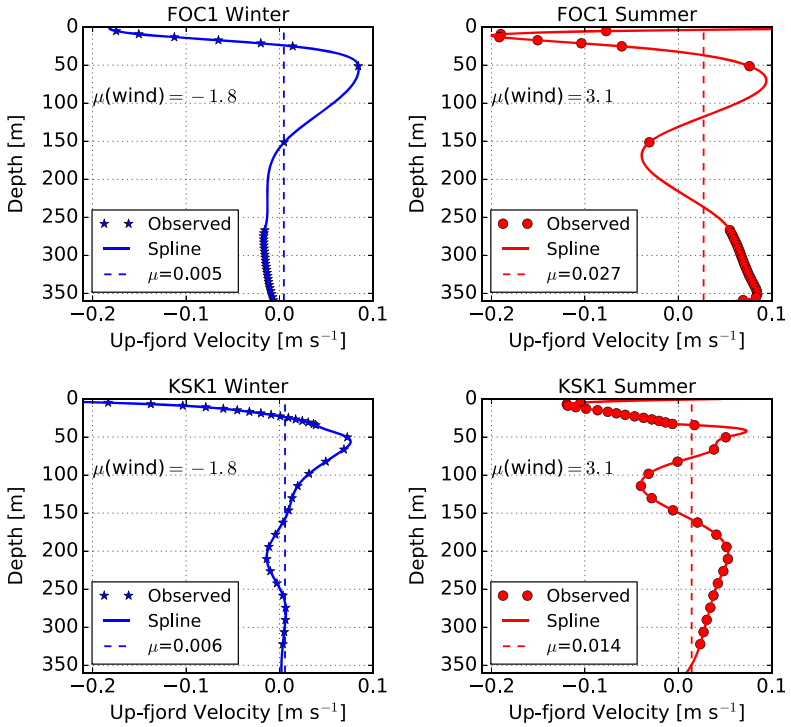

Figure 5. Seasonal mean along-channel velocity at Station FOC1 (53.736°N, 129.030°W) and KSK1 (53.480°N, 129.209°W) in Douglas Channel. The observed mean velocities are averaged after applying the low-pass filters, the solid lines are the cubic splines fitted to the observed mean velocities, and the dashed lines (μ values) are the vertically averaged velocity from the surface (0 m) to the bottom (360 m) computed from the spline fits. μ(wind) is the averaged along-channel wind velocity during each time period in the channel.

In contrast to other well-studied shallow-silled inlets (e.g., Knight Inlet by *Baker and Pond* [1995]), the renewal water from the shelf is dense enough to reach the bottom of both basins in Douglas Channel, but the strongest velocity is at about 200 m depth, below the sill at the shelf at about 140 m depth, for the outer

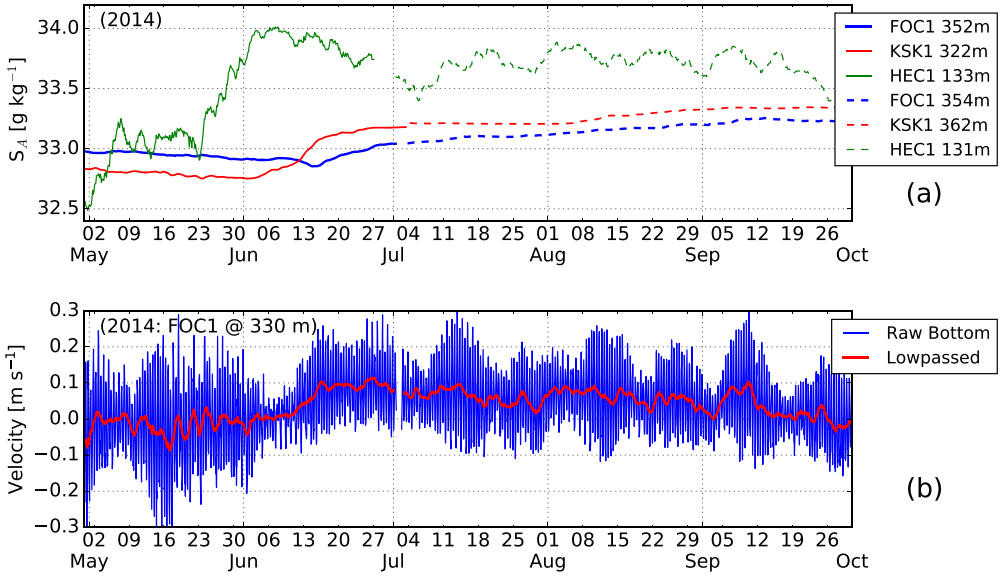

Figure 6. (a) Absolute Salinity at the bottom of the three stations during the renewal in 2014. (b) Bottom along-channel velocities (raw and low-passed) at FOC1 during the renewal in 2014. The bottom current meter at KSK1 failed on 10 May 2014, so there are no bottom current observations in the outer basin that captured this summer renewal process. The salinity time series during renewal periods are also included in supporting information Figures S2 and S3.

basin, and likely deeper toward the bottom for the inner basin. Furthermore, the inflow does not seem to be interrupted by either the spring or the neap tide (Figure 6)—the mixing at the inner sill is not strong enough to inhibit the renewal flow even during spring tide, and the kinetic energy that is provided by the relatively weak neap tide is enough to lift the dense water over the sill. In fact, the velocity at depth at FOC1 is in the up-fjord direction even during some relatively strong ebb tides (approximately from 20 June to 4 July 2015 at FOC1, Figure 6).

There are a few interesting points in the salinity time series (Figures 2e, 6 and supporting information Figures S2 and S3) that influence the estimate of the time it takes for the renewal water to go from KSK1 to FOC1. It is clear that the deep salinity at KSK1 starts to increase on 4 June 2014 and it starts to increase at FOC1 on 14 June 11 days later. However the salinity at KSK1 (322 m) starts lower than at FOC1 (316 and 352 m), and does not exceed the salinity at FOC1 until about 11 June. The salinity at FOC1 starts to increase on 14 June, 3 days later, simultaneously at 316 and at 322 m depths. In 2015, we only have the salinity measurement at KSK1 at 362 m, which is 40 m deeper than the one in 2014, and the salinity is always higher than the ones at FOC1 (297 and 354 m). The bottom salinity at KSK1 at 362 m depth started to increase on 1 May 2015. Three days later, the salinity at 297 m starts to increase; the salinity at FOC1's deeper depth (354 m) starts to increase 10 days later on 11 May. The two deep salinity time series at FOC1 then increase at the same rate. In addition, there is a curious sudden increase followed by a decrease in salinity at FOC1 at 352 m depth right before the renewal that is not present in 2015, which we cannot explain at this point.

The picture we draw is as follows. When the high density water appears at depth at HEC1, this water starts to flow over the sill at the shelf and fill the outer basin of Douglas Channel. This water then needs to fill the basin from the bottom up until dense water is able to get over the inner sill. Once this water starts to flow over the sill it continues to do so until the dense water disappears from HEC1 (late September). Our observations and analysis do not allow us to determine whether the water crosses the inner sill at all phases of the tide, but the observations at FOC1 suggest that the renewal flows are not interrupted by spring or neap tides. The question of how long it takes for the renewal water to get from KSK1 to FOC1 does not have a simple answer because of the need for the renewal water to fill the outer basin. In 2015, it is clear that the renewal water appears at FOC1 on 4–5 May. However, it is not clear whether to start the clock when the renewal water arrives at KSK1 (297 m) and the salinity starts to increase or when the water at KSK1 (297 m) is dense enough to reach the bottom at FOC1. The range of time estimates is 3–10 days which gives a range of speeds of 3–13 cm s^{-1}.

Given the above evidence, we argue that the dense water flows over the inner sill into the inner basin is driven by density difference between the deep water in the outer and the inner basins. *Benjamin* [1968] derived the solution for the gravity current speed for steady density currents:

$$c=\left[\frac{(H-d)(2H-d)}{H(H+d)}\right]^{1/2}\sqrt{g'd}, \tag{1}$$

where H is the water depth (360 m), d is the bottom layer thickness (130 m for FOC1), g' is the reduced gravity ($g\Delta\rho/\rho$), and $\Delta\rho$ is the density difference between the ambient density and the intrusion density. To estimate velocity c, we assume the ambient density is the potential density at FOC1 at 316 m, with a 2 day time lag (estimated transit time from the sill to FOC1), and the intrusion density is the potential density at KSK1 at 322 m less 0.12 kg m^{-3}, which is approximately the density difference between the sill depth (200 m) and the observed depth according to the CTD data from July 2014 cruise. The estimated intrusion velocity is then c=0.05 to 0.19 m s^{-1} (from 15 June to 28 June 2014 estimates), which is consistent with the observed bottom velocity (0.10 m s^{-1}, from 15 June to 28 June 2014 in Figure 6, noting the rapidly increasing velocities before 15 June). These estimates are also consistent previous estimate of 3–13 cm s^{-1} from the salinity time series. This estimation is sensitive to (1) the estimate of the bottom layer thickness at FOC1, which relied on the spline fit between 150 and 260 m because the lack of data; (2) and the estimated intrusion density does not account for the mixing at the sill and entrainment between KSK1 and FOC1. Nevertheless, the consistency between various speed estimates support the idea that the renewal water that cascades the inner sill takes the form of gravity currents at the bottom of the inner basin. Similar gravity current intrusions have also been reported in Puget Sound [*Geyer and Cannon*, 1982] and in the Strait of Georgia [*Masson*, 2002].

One usually expects a gravity current to arrive with a sharp front, and this feature has been seen in some fjords. For example, in the basin of Gullmar Fjord, Sweden [*Arneborg and Erlandsson*, 2004], the dense water filled the bottom 36 m in less than 24 h in April 2002. For the Douglas Channel system, the rapid increase of the salinity takes about 10 days for the deep water at FOC1 and KSK1. This is consistent with the deep salinity signal at HEC1. We speculate that the smooth increase in the salinity at KSK1 is a reason that a sharp front is not observed at FOC1.

Although beyond the scope of this paper, we also note that the salinity difference between HEC1 and KSK1 is due to the mixing that occurs between the two. The outer sill at the mouth of the Douglas Channel is not a clearly defined sill, but an about 26–30 km wide extended region that connects with the continental shelf (at about 140 m depth). The mixing before the water enters to Douglas Channel could greatly reduce the density of this dense water, whose density gradually increases. This intense mixing at the mouth is supported by the density difference (0.5–1.0 kg m^{-3}) between the HEC1 bottom water and the basin water densities. This type of gradual salinity change (5–7 days) was observed in Puget Sound, which has a 30 km extended sill at the entrance [*Geyer and Cannon*, 1982].

4. Wind-Driven Response

Surface wind-driven currents in fjords have been reported in numerous studies. Wind stress is able to enhance or reverse the surface estuarine outflow [e.g., *Matsuura and Cannon*, 1997 in Puget Sound; *Baker and Pond*, 1995 in Knight Inlet; *Castillo et al*., 2012 in Reloncavi Fjord], and counter-currents at depth were also observed in these fjords (e.g., at around 100 m in Puget Sound by *Matsuura and Cannon* [1997]). Next we explore the relationship between the low-passed wind and current velocities in Douglas Channel.

4.1. Wind-Driven Currents

Simple linear regression analysis between the low-passed along-channel wind velocity and the along-channel current velocity at 5 m at FOC1 shows that the surface current velocity is highly correlated with the wind velocity (current velocity lags the wind by 5 ± 20 h, $r^2 = 0.63$):

$$u_{F@5m} = 0.027W - 0.14 \text{ m s}^{-1}, \tag{2}$$

where W is the up-fjord wind velocity during this time period (13 January to 25 July 2015). This simple regression clearly distinguishes the estuarine outflow and the wind-driven currents. During this time period, the estuarine circulation contributes to an average of 0.14 m s^{-1} outflow, and the mean wind ($\bar{W} = 0.88$ m s^{-1} up-fjord) contributes to an average of 0.024 m s^{-1} inflow (0.027×0.88 m s^{-1}), so on average, the net outflow is 0.12 m s^{-1}. For this period, the wind variation can explain 63% of the velocity variation, and the amplitude of the current velocity variation is about 2.7% of the wind velocity variation. This surface current and wind regression coefficient is relatively robust during other time periods (between 2.2% and 3.7%, supporting information Table S1) with some exceptions. These results are roughly consistent with *Weber* [1983], who showed analytically that the total surface currents should be between 3.1% and 3.4% of the wind speed. The uncertainty is calculated at the 95% significance level, and the effective degrees of freedom are computed as $N/67$, where N is the number of the hourly samples and the energy amplitude drops to half at $T = 67$ h after the Godin filter.

To provide information about the very near surface currents for pollutant spill applications, we use the regression relationships for the upper three bins for FOC1 and KSK1 to extrapolate the relationships to the surface:

$$u_{F@0m} = 0.049W - 0.14 \text{ m s}^{-1}; \tag{3}$$

$$u_{K@0m} = 0.052W - 0.23 \text{ m s}^{-1}. \tag{4}$$

The density driven components are different for these two stations, but the wind-driven components are roughly the same, around 5% of the wind velocity. These relationships will be tested later in future studies using drifter data collected during this observing program.

The above relations between the wind velocity and the current velocities can be used as a proxy to estimate the current velocities when direct measurements are not available, assuming that the relations are stable

over time. Our analyses show reasonably consistent correlations between the wind and the surface current velocities during all available time periods (supporting information Table S1). The root-mean-square deviation (rmsd) can be used as a measure of the difference between the estimator and the actual observations here. The prediction results are reasonable for the surface current velocity. The rms of the observed surface current velocity during this time period (13 January to 25 July 2015) is 0.18 m s^{-1}, and the rmsd of the predicted surface (5 m) current velocity by equation (2) during this time period is 0.09 m s^{-1}. During all available time periods listed in supporting information Table S1, the rmsd of the predicted velocities are generally around 0.1 m s^{-1}. Overall, it is relatively robust to use the wind to estimate the subtidal surface current velocities, and the estimated velocities are generally 10% smaller than the observed velocities.

4.2. Surface Slope Response

We next analyze the wind response in terms of the sea surface slope in the fjord. In a long narrow channel, the sea surface is set up in response to wind-forcing, which allows us to estimate the thickness of the layer directly influenced by the wind. Assuming the vertical mixing coefficient in the wind-influenced layer is constant, the steady state vertically integrated momentum balance for the wind-influenced layer, h_1, that is directly subject to wind influence is [*Farmer*, 1976]:

$$\tau_w - \tau_{h_1} = h_1 \rho_1 g \frac{\partial \eta_1}{\partial x} \tag{5}$$

with $\tau_w = \rho_{air} C_d W|W|$ and $\eta_1 = \eta_k - \eta_h$, where τ_w is the surface stress, C_d is the surface drag coefficient (1.2×10^{-3}, *Large and Pond* [1981]), ρ_{air}=1.2 kg m^{-3} is the air density, ρ_1=1010 kg m^{-3} is the averaged density of the wind-influenced layer, g is the gravitational acceleration, W is the up-fjord wind velocity, x is the along-fjord axis, τ_{h_1} is the stress at the base of the wind-influenced layer, and η_k and η_h are the sea surface elevations observed at Kitimat and Hartley Bay, respectively (Figure 1). Kitimat and Hartley Bay are 80 km apart, so the barotropic pressure gradient term ($\partial\eta_1/\partial x$) can be approximated as $(\eta_k - \eta_h)/80$ km.

The steady state approximation is reasonable as the gravity wave speed in 300 m of water is 54 m s^{-1} and signals will propagate from one location to the other in less than 30 min. This is fast compared to the subtidal frequencies in the filtered time series.

Now we decompose equation (5) into the time-constant and time-varying components, denoting them as $\bar{(\cdot)}$ and $\tilde{(\cdot)}$, respectively. Under the assumptions that the wind-influenced layer thickness h_1 is constant (i.e., $\tilde{h}_1 \ll \bar{h}_1$ so $h_1 \approx \bar{h}_1$), and $\tilde{\tau}_{h_1}$ is independent of h_1 (Figure 5 shows approximate linear stress in the upper 50 m depth), h_1 can be determined from the slope of the linear regression relationship between the time-varying components of the wind stress and the sea surface slope:

$$\tilde{\tau}_w \sim h_1 \rho_1 g \frac{\partial \tilde{\eta}_1}{\partial x} \tag{6}$$

and the mean bottom shear stress of the wind-influenced layer can then be estimated through the time-constant balance:

$$\bar{\tau}_{h_1} = \bar{\tau}_w - h_1 \rho_1 g \frac{\partial \bar{\eta}_1}{\partial x}.$$

For the period 13 January to 25 July 2015, the correlation between the wind stress and the barotropic pressure gradient is large and is statistically significantly different from 0 (r^2=0.74 where the pressure gradient lags the wind by 5 ± 9 h). The r^2 for the other time periods ranged from 0.72 to 0.77 (see supporting information Table S2). The maximum lagged correlations between the wind stress and the individual sea level time series are much smaller and not significant (r^2=0.17 and 0.22 at Kitimat and Hartley Bay, respectively). The strong correlation between these two terms indicates that more than 70% of the variation in the barotropic pressure gradient variation can be explained by the wind variation, which also indicates that the contribution of the wind stress to the $\tilde{\tau}_{h_1}$ is small because $\tilde{\tau}_{h_1}$ is determined by the background time-varying density driven flow. Nonetheless, we only focus on the wind stress and the surface pressure gradient relationship here.

From the regression, we get h_1=8.0±1.1 m. The estimations for h_1 are between 8 and 12 for all time periods that we have available (supporting information Table S2). This 8 to 12 m wind-influenced layer

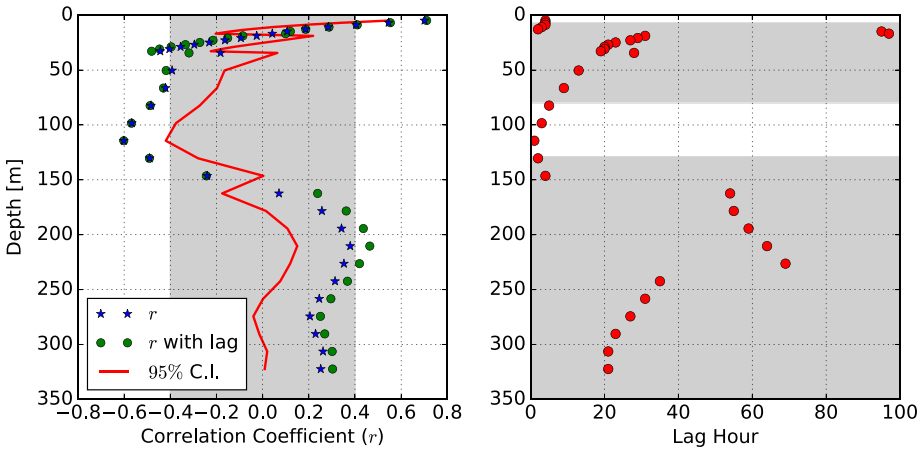

Figure 7. (left) Correlation coefficients *r* (blue stars) between the along-channel wind velocity and the along-channel current velocities measured at KSK1. (right) The time lags for the along-channel wind velocity and the along-channel current velocity to reach the maximum correlation (the green circles in the left plot are the maximum correlation coefficients given the corresponding time lags). The 95% confidence limit for *r* is labeled in the red line (i.e., when the absolute value of the red line is larger than 0, it is considered as statistically significant but not necessarily practically significant). The regions where *r* is within $[-0.4, 0.4]$ (i.e., $r^2 < 0.16$) are considered practically not significant for this study and shaded in gray. The time period chosen for this analysis is from 13 January to 25 July 2015, where we have continuous concurrent current velocity and wind observations.

thickness is consistent with the rapid decrease with depth of the correlation coefficient between the wind and currents as evident in Figure 7. It is also consistent with the approximately 10 m thickness of the surface water seen in the salinity profiles (Figure 9).

4.3. Barotropic and Baroclinic Response

The analysis so far has focussed on the surface response to the wind. However when an up-(down-)fjord wind increases (decreases) sea level at the end of the fjord this will depress (raise) the isopycnals. These changes in isopycnal depth can cause a baroclinic response in the density field, which propagates down-fjord and affects the currents [*Farmer*, 1976; *Matsuura and Cannon*, 1997].

Figure 7 shows the correlations between the wind and the currents through the water column at KSK1 for the period 13 January to 25 July 2015. The correlation coefficient *r* drops rapidly from 0.7 near the surface to zero at about 20–50 m; it has a negative maximum of −0.6 at about 115 m depth; *r* crosses zero and becomes a small positive number below 150 m. The negative correlation between the wind and the current in the 100 m depth band was also reported in other inlets. *Matsuura and Cannon* [1997] found the negative maximum correlation occurred at 100–120 m depth in Puget Sound, and a weak wind-induced velocity response was reported near the bottom (below 100 m) in Knight Inlet [*Baker and Pond*, 1995].

The lagged correlation between the fluctuations in the wind and the near-surface potential density difference between KSK (at 15 m) and FOC (at 12 m) has $r^2 = 0.45 \pm 0.19$ with lag $= 16 \pm 22$ h (for the period 13 January to 25 July 2015 at the 95% significance level; see supporting information Table S3 for results during other time periods), which suggests the potential for a baroclinic response. The first mode baroclinic wave has a speed of 0.8 m s^{-1}, so the travel time from Kitimat to KSK is about 24 h, which is consistent with the observed lag.

The counter-wind current velocity at 115 m depth is in the same direction as the barotropic pressure gradient, indicating the importance of the barotropic response. Given the potential baroclinic response, the dynamics requires that we consider both. The linearized momentum equation in the along-channel direction at depth *z* below the direct wind-driven layer, with forcing terms being the barotropic and baroclinic pressure gradients is:

$$\frac{\partial u}{\partial t}|_z = -g\frac{\partial \eta_1}{\partial x} - \frac{g}{\rho_0}\int_z^{\eta}\frac{\partial \tilde{\rho}}{\partial x}dz \tag{7}$$

where $\tilde{\rho}$ is the perturbation component of the density, and ρ_0 is a reference density. The first term on the rhs is the barotropic pressure gradient at depth z and the second term is the baroclinic pressure gradient.

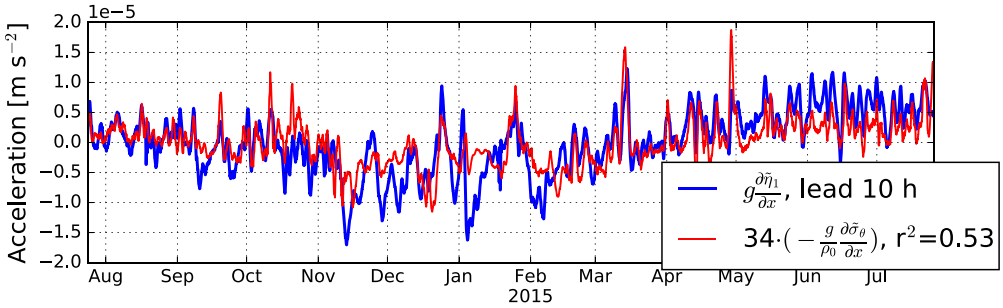

Figure 8. Time series of the barotropic ($g\frac{\partial\eta_1}{\partial x}$, blue) and baroclinic ($-h_1\frac{g}{\rho_0}\frac{\partial\tilde{\sigma}_\theta}{\partial x}$, red) forcing terms. These two time series are correlated ($r=0.73\pm0.07$), and the fitted coefficient of the linear fit is 34 ± 6 m corresponds to the depth at which these two forcing terms balance each other. The peak correlation occurs when the elevation difference lags the density difference by 10 ± 18 h (95%).

While it is not possible to directly measure the baroclinic pressure gradient given what we have, we will assume that the density gradient anomalies at 12 m at FOC1 and at 15 m at KSK1 gives a reasonable averaged values for the upper 30–50 m for the baroclinic gradient term. Then we can estimate at which depth these two terms balance each other by setting the lhs of equation (7) to 0, and perform a linear regression to find z. The linear fit (Figure 8) results show these two pressure gradient terms balance each other at 34 ± 6 m.

The barotropic and baroclinic pressure gradient terms compete with each other at all depths. However, because the barotropic pressure gradient does not vary with depth, we hypothesize that the rich vertical profile of the correlation coefficient between the velocity and the wind (Figure 7) is ultimately the result of the vertical profile of the baroclinic pressure gradient term.

Below the direct wind-influence layer (top 10 m or so) where the wind stress dominants the velocity, the baroclinic term starts to become important, and is comparable with the barotropic pressure gradient at 30–40 m. This is consistent with the insignificant correlation coefficients between the wind and the current velocities at 20–40 m depth, where the wind induced barotropic and baroclinic forcings counter balance each other.

Between 50 and 150 m depths, the current velocity is in the direction of the barotropic pressure gradient (counter-wind direction), which suggests that the adjusted isopycnals below 34 m depth cause the baroclinic term to be insignificant at middepth or significant but in the same direction as the barotropic pressure gradient. Therefore, the currents in the 100 m depth band seem to be driven by the barotropic pressure gradient. As it goes deeper than 150 m, the baroclinic pressure gradient opposes the barotropic pressure gradient again, and reaches its peak at 200 m depth. Given our limited observational data, we cannot say for uncertain at this point whether the baroclinic pressure gradient agrees with the correlation vertical profile, but this will be investigated more carefully with numerical experiments along with analytical solutions in our future studies.

5. Volume Budget and the Surface Outflowing Layer

5.1. Volume Budget

The velocity profiles shown in Figure 5 provide us a way to look at the volume transport of each velocity "layer." Here we follow examples in other fjord studies [e.g., *Baker and Pond*, 1995] and define the "layers" as the inflowing and the outflowing water masses. The volume transport of each layer can then be calculated under these assumptions: the cross-sectional velocity and density variation is negligible; the velocity measured by the ADCPs and interpolated by the spline fit is a good representation of the overall along-channel flow; the cross-sectional width is parameterized as a function of depth instead of having uniform width at each depth to minimize the error that could be introduced by the bathymetry (details are given in Table 2).

Under these assumptions, the volume transport for each "layer" is then calculated at FOC1 and KSK1 for both the summer renewal and the winter seasons (Table 2). Layers 1 and 2 represent the outflowing and the inflowing layers in classic estuarine circulation. The surface outflow (Layer 1) has similar volume

Table 2. Volume Budget at FOC1 and KSK1[a]

	KSK1 Summer		FOC1 Summer		KSK1 Winter		FOC1 Winter	
Layer	Depth (m)	10^3 (m^3 s^{-1})	Depth (m)	10^3 (m^3 s^{-1})	Depth (m)	10^3 (m^3 s^{-1})	Depth (m)	10^3 (m^3 s^{-1})
0	0	0.236	0–3	2.046				
1	1–33	−10.903	4–32	−11.524	0–22	−13.448	0–23	−10.300
2	34–82	9.405	33-131	19.105	23–169	22.206	24–158	22.142
3	83–149	−7.241	132–233	−5.263	170–248	−2.087	159–360	−4.287
4	150–360	19.689	234–360	11.798	249–360	1.067		
Net	0-360	11.186	0-360	17.304	0-360	6.864	0-360	7.555

[a]Negative numbers represent seaward flow, and positive numbers represent landward flow. The cross-channel widths (w_f for FOC1 and w_k for KSK1) at these two stations are parameterized as a function of depth (d): $w_f(d) = -7.7 \cdot d + 3770$ m, $w_k(d) = -10.2 \cdot d + 5286$ m, with d going from 0 to 360 m (results are from linear fits). The volume transport of each layer is then calculated by integrating the velocity profile (obtained from the cubic spline fits, Figure 5) over the cross-sectional area of the corresponding layer, assuming no cross-channel variation. The cross-sectional areas for FOC1 and KSK1 are 860,000 m^2 and 1,242,000 m^2, respectively.

transport at both moorings in both summer and winter (around 10×10^3 m^3 s^{-1}). The summer outflowing layer is 10 m thicker than the winter outflowing layer (30 m compared to 20 m). Layer 2 has similar volume transport (around 20×10^3 m^3 s^{-1}) and thickness between the moorings in winter. In summer, the transport of Layer 2 at KSK1 is reduced by a factor of about two (around 10×10^3 m^3 s^{-1}), whereas Layer 2 at FOC1 does not show this difference. Layer 0 represents the inflowing layer above Layer 1. A relatively small transport layer is present in summer at both stations (in the order of 1×10^3 m^3 s^{-1}), which is a consequence of the summer up-fjord wind.

At KSK1, the data density of the velocity profile is sufficient to constrain the spline fit. However, this is not true at FOC1 where between 50 and 250 m there are only data points at 50 and 150 m. The spline profile gives very similar layer thicknesses at KSK1 and FOC1 in the winter but very different ones in the summer. We note that in the upper 200 m, the spline fit at KSK1 is reasonably consistent with the data points at FOC1 for both winter and summer. In winter the measurements at 150 m at FOC1 happened to define the location of the bottom of layer 2 which was consistent with that observed at KSK1. However, in the summer the data at FOC1 does not define the velocity profile zero crossings and the spline profiles in the upper 200 m at FOC1 and KSK1 are very different.

There is a strong argument that the transport in Layers 1 and 2 (the two estuarine flow layers) should be reasonably continuous between FOC1 and KSK1 since there are no substantial side channels to act as sources or sinks. In addition, the fact that the winter profiles are very similar down to 200 m indicates that the sill at 200 m depth between the two moorings is not a major source of mixing that alters the thicknesses of the upper two layers.

If Douglas Channel did not have any side channels, the "net flux" term in the volume budget would be a small negative number representing the freshwater moving down the fjord; however, in Table 2 the "net flux" term is comparable in size to the layer transports and directed up-fjord (positive). Cross-channel variation is often invoked to explain volume transport discrepancies when studying circulation in fjords and inlets [*Halverson et al*., 2013], because the along-channel flow can be under-resolved given the limited measurement across the channel. It is even considered as a significant contributor in some "narrow" channels. For example, *Baker and Pond* [1995] concluded that the cross-channel circulation might be more important than anticipated even in Knight Inlet, even though it is a "narrow" channel. However, the complexity of the channel network in the Kitimat region gives us another possible explanation for the "net flux."

Using simple numerical models, *Webster* [1980b] suggested that the interpretation of the flows in Douglas Channel in terms of estuarine flow requires that we consider Gardner Canal and Verney Passage and account for the freshwater flux out of the system via Verney Passage (Figure 1). Following this postulation, assuming Layer 2 in Douglas Channel provides all of the required salt flux and the salinity of hypothesized outflowing surface layer in Verney Passage is comparable with the outflowing surface layer in Douglas Channel, we can use the standard estuarine flow equations (*Knudsen* [1900] as cited by *Freeland and Farmer* [1980]) to estimate the freshwater flux to see if it gives us a reasonable range: $Q_f = Q_1(S_2 - S_1)/S_2 = Q_1(1 - S_1/S_2)$, where Q_1 is the volume flux out at the surface, S_1 is the average salinity in the outflowing surface layer and S_2

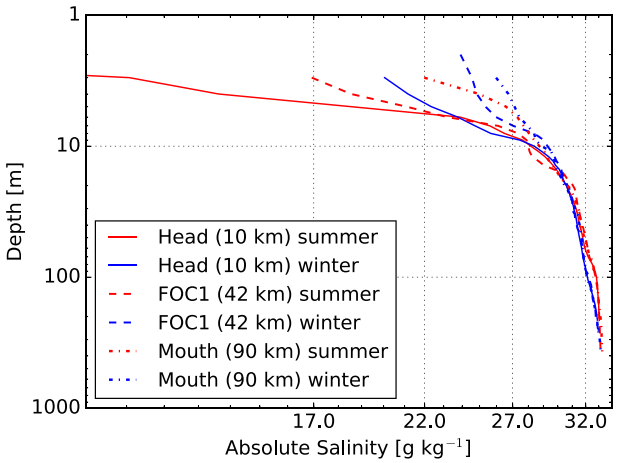

Figure 9. Absolute Salinity at the head (solid lines), FOC1 (dashed lines) and at the mouth (dash-dotted lines) of Douglas Channel. The summer data are the average of the July 2013 and July 2014 cruise CTDs, and the winter data are the average of April 2014 and October 2014 cruise CTDs. The vertically averaged Absolute Salinities (in g kg^{-1}) for layers 1 and 2 at the head are: S_1(summer)=28.41, S_2 (summer)=31.94; S_1(winter)=27.75, S_2 (winter)=32.02; at FOC1: S_1(summer)=29.00, S_2(summer)=32.09; S_1(winter)=28.80, S_2 (winter)=32.05; at the mouth: S_1(summer)=30.02, S_2(summer)=32.00; S_1 (winter)=29.02, S_2 (winter)=32.03.

is the average of the deep salinities. Taking S_2=32 g kg^{-1} (the salinity at 100 m in Figure 9) and S_1=29 g kg^{-1} or 30 g kg^{-1} (the salinity at 10 m at the mouth Figure 9), this yields freshwater flux estimates between $[1.2, 1.9]\times 10^3$ m^3 s^{-1}, which matches *Morrison et al*. [2012] at the lower bound.

Therefore, the hypothesis, that at least some of the net flux terms in Table 2, represents the volume flux required to supply the surface outflow at Verney Passage is not unreasonable. This hypothesis also reduces the need for horizontal or vertical recirculation patterns to balance the volume fluxes at KSK1 and FOC1. Making sense of this will require a more complete regional analysis of the temperature and salinity properties, and a numerical circulation model that includes all channels and possible strong mixing at channel junction points.

5.2. Surface Outflowing Layer Thickness

The forgoing analysis suggests that it is the freshwater discharge and the salinity distribution that control the surface transport. But what controls the outflowing surface layer thickness in this system, and in particular, why is the surface layer 10 m thicker in summer than that in winter (Table 2)?

The potential density profiles show that the brackish water is mostly in the top 5–7 m, and the depth of maximum negative curvature in the salinity (Figure 9) and the potential density (supporting information Figure S1) profiles is generally around 6–10 m, which is similar to what *Webster* [1980b] obtained from the cruise CTD profiles (10–14 m). However, the velocity ADCP shows that the surface outflow layer is consistently around 30 m thick in summer, and highly variable in winter (Figure 4).

An estimation of the surface freshened layer thickness can be made by examining the balance between the wind stress and the density driven flow by the Wedderburn number (*Wb*) [*Farmer and Freeland*, 1983; *Geyer*, 1997; *Inall et al*., 2015],

$$Wb=\frac{\tau_w L}{\Delta\rho g H_1^2}, \tag{8}$$

where $\tau_w=\rho_{air}C_d W|W|$ is the wind stress, L is the length of the fjord (80 km in Douglas Channel), and $\Delta\rho$ is the upper layer density difference along the fjord axis. Because we know the wind-driven influence at the surface is comparable with the density driven force (e.g., in Figure 5 the wind is able to reverse the surface flow in summer), we set Wb = 1 to estimate the thickness of the outflowing surface layer (H_1):

$$H_1=\sqrt{\frac{\tau_w L}{\Delta\rho g}}. \tag{9}$$

In Douglas Channel, $\Delta\rho$=1.6 kg m^{-3} in summer between the head and the mouth, and $\Delta\rho$=1.0 kg m^{-3} in winter; the values are obtained by averaging the winter (April and October) and the summer (two Julys) the CTD profiles. The predominantly up-inlet wind in summer at 3.1 m s^{-1} on average gives H_1=28 m, and the predominantly down-inlet wind in winter at 1.8 m s^{-1} on average gives H_1=6 m. The surface density is averaged over the approximate first velocity layer (35 m in summer and 25 m in winter). If we only consider the surface 10 m for the surface density, the estimated values are H_1=6 m in summer ($\Delta\rho$=4.0 kg m^{-3}) and H_1=4 m in winter ($\Delta\rho$=2.6 kg m^{-3}). These estimates are 1/5 to 1/3 of the measured thicknesses (recall

Table 2: about 32 m in summer and 22 m in winter), indicating that $Wb = 1$ is an overestimation so the density-driven flow dominants over the wind-driven flow at the surface on average.

Up-fjord and down-fjord winds can have different effects in addition to the undirectional estimates above. An up-inlet wind tends to thicken the surface outflowing layer at the head of an estuary and to retard the surface outflow, whereas a down-inlet wind tends to blow the outflowing surface layer water out and enhance the estuarine exchange [*Farmer and Osborn*, 1976; *Farmer*, 1976; *Inall et al*., 2015].

In Douglas Channel the surface outflowing layer thickness can be much different than the mean conditions. When the mean wind direction changes from up-fjord to down-fjord (e.g., mid-September to late-October in 2014, Figure 2), the surface outflow layer thickness is generally less than 10 m (e.g., Figure 4, mid-September to late-October in 2014), which agrees with the stratification layer thickness. During high wind stress events, the wind stress influence dominates the density-driven flow in the outflowing surface layer ($W_b = [12, 1]$ given $H_1 = [10, 50]$ m, and $W = 15$ m s^{-1}). The peak wind in Douglas Channel is mostly down-fjord, so we see the deepened (to 50–70 m) surface enhanced outflowing surface layer that is driven by the wind stress (early December 2014 and early January 2015 in Figure 4), and a compensating inflow layer immediately underneath it.

The near surface stratification in Douglas Channel will inhibit convectively generated turbulence in the outflowing surface layer [*Farmer and Freeland*, 1983], but other mixing processes, such as wind mixing, can generate turbulence and entrain the underlying water into the surface outflowing layer [*Stigebrandt*, 2012]. Now we explore whether the outflowing surface layer is controlled by the wind mixing from dynamics.

The mechanistic model that *Stigebrandt* [1981] presented for a stationary surface layer suggested that, in deep stratified fjords, the thickness of the surface outflow layer is controlled by three factors: the wind mixing, the freshwater discharge, and the mixing at a hydraulic control point. In Douglas Channel, there is no obvious location along the channel that provides a horizontal or vertical constriction acting like a hydraulic control point. So the hydraulic effects are not expected to be significant. This allows us to focus on the wind-influence component [*Stigebrandt*, 1981, 2012]:

$$H_1(W, Q_f) = a \cdot \frac{W^3}{Q_f}, \tag{10}$$

where W is the wind speed, Q_f is the freshwater discharge, and $a = \frac{C_e A_f}{2M}$, with $C_e = 2.5 \times 10^{-9}$ being an empirical constant that incorporates the drag coefficient on the air-sea interface, A_f being the area subject to wind mixing, and $M = g\beta S_2$ (g is the gravitational acceleration, β is the salinity contraction coefficient: 0.0008 (g/kg)$^{-1}$, and S_2 is the salinity of the second layer).

The averaged layer thickness estimate from equation (10) is only 1.4 m in winter, and even smaller (0.6 m) in summer. These estimates are one order of magnitude smaller than those calculated from the velocity profile. Furthermore, even if we expand the wind-influenced surface area to include Gardner Canal and the connecting passages (i.e., increase A_f from 380 to 811 km^2), the estimated thickness will still be one order of magnitude smaller and the greater thickness in summer will still not be explained. The estimated wind component of the first layer thickness is able to capture the sudden peaks shown in winter (Figures 3 and 4) of up to 28 m, but still 50% smaller than observed in Figure 4 in December and early January.

Other mixing processes may be more or equally important than wind mixing in determining the surface brackish water thickness. Examples include side-wall mixing, internal waves, horizontal entrainment at the intersections of two or more channels, and possible mixing from the internal lee wave formed on the downstream side of the sill during both flood and ebb tides over the 30 m deep sill in Verney Passage [*Webster*, 1980b]. However, we do not have any evidence to pursue this.

Therefore, the outflow layer thickness is greatly influenced by the wind energy input to the surface water through processes captured by the Wedderburn Number. These processes are able to explain the thicker velocity outflow layer as compared to the pycnocline, the relatively constant thickness in summer seasons, the much thinner layer during wind direction transition periods, and the much deepened outflow layer (50–70 m) influenced by wind during winter storm events. This hypothesis will be further investigated using numerical models in future research.

6. Discussion and Summary

6.1. Seasonal Circulation

The dominant feature of the seasonal circulation in Douglas Channel is a four layer circulation in summer (May/June to September) and a three layer circulation in the winter (October to May/June). In both seasons the upper two layers are estuarine-like with a relatively fresh surface outflow layer and a saltier inflow layer immediately below. The mean surface outflow is approximately the same in summer and winter (10×10^3 m^3 s^{-1}) at both KSK1 and FOC1. In summer the volume transport in the second (inflow) layer is approximately in balance with the surface outflow (as expected for estuarine flow) at KSK1, however in winter the transport in the second layer is estimated to be 20×10^3 m^3 s^{-1} (at both KSK1 and FOC1), about twice of what is required to balance the surface outflow.

The summer Layer 2 thickness and transport at FOC1 are questionable because of the vertical resolution, where between 50 and 250 m there are only velocity data points at 50 and 150 m. Since there are no substantial side channels between FOC1 and KSK1 to act as sources or sinks and the sill between them is much deeper than the bottom of the second layer, we expect that the transport of the surface two layers at the moorings to be in a reasonable agreement. At KSK1 the vertical resolution of the velocity profile is sufficient to constrain the spline fit (Figure 5). In winter the measurements at 150 m at FOC1 happened to define the location of the bottom of layer 2 which was consistent with that observed at KSK1. However in summer the data at FOC1 does not constrain the velocity profile zero crossings, so we face a more significant spatial aliasing problem here. Therefore, the spline fit and the velocity profile at FOC1 in summer could be more misleading than informative.

The mean surface outflow layer thickness is about 30 m thick in summer (at KSK1) and only about 20 m thick in winter. The scaling analysis based on the Wedderburn number (*Wb*) indicates the thicker surface outflow layer in summer is due to the larger magnitude of the mean wind. The second layer (inflow) also shows substantial differences between seasons; at KSK1 it extends from about 30 to 80 m depth in summer, whereas it extends from about 20 to 170 m in winter. This thicker winter inflow layer, which delivers shelf water into Douglas Channel, was inferred by *Macdonald* [1983] from the water properties.

In summer, below the surface estuarine circulation, there is a season long renewal event with inflow at the bottom and an outflow above that. This deep inflow is caused by the appearance of dense water at depth at the entrance to the fjord system which cascades through the system until it disappears from the entrance, at the speed of $0.1 - 0.2$ m s^{-1}, which is consistent with gravity currents. The timing of the dense water appears to be related to the regional transition on the British Columbia coast from a downwelling regime to upwelling in May/June and then back to downwelling in September. In winter, the deep flows in the inner basin (FOC1) are directed outwards over at least the bottom 60 m, whereas in the outer basin there is an outward flow centered at about 200 m (the inner sill depth).

The salinity of the deep water in the basins is dictated by the summer renewal signal. The deep salinity increases during renewal season, most rapidly in the first 10 days. It decreases gradually from the end of the renewal until it starts again next year, which indicates that diffusion and entrainment are the dominant mixing processes in the deep basin in winter. This gradual change in salinity between renewals was also observed in the deep waters between renewals in Strait of Georgia [*LeBlond et al*., 1991; *Masson*, 2002] and Indian Arm [*de Young and Pond*, 1988].

The multilayer circulation observed in Douglas Channel is not unique. A multilayer structure with an estuarine circulation overlaying a complex deep water circulation was observed in the inner basin in spring 1988 and in the outer basin in summer 1989 [*Baker and Pond*, 1995]. However, during the same time periods, the complex structure was not observed in the other basin (the outer basin in spring 1988 and the inner basin in summer 1989). The difference in layer structures between the basins is much larger than in Douglas Channel, which is attributed to stronger mixing over the shallow sills in Knight Inlet.

Deep water renewals are studied in many fjords, such as in Puget Sound [*Geyer and Cannon*, 1982], Indian Arm [*de Young and Pond*, 1988], Knight Inlet [*Baker and Pond*, 1995], and Strait of Georgia [*Masson*, 2002]. They focused on how the spring/neap tidal cycle controls the renewal events once the dense water becomes available at the mouth. For example, in Knight Inlet, the enhanced mixing at the outer shallower sill (64 m) inhibits the intrusion, so the renewal signal is observed during the less energetic tides (neap

tides); the deep water renewal of the inner basin requires the more energetic spring tides for the dense water to go over the relatively deeper sill (68 m), and the return flow is observed both above and below the deep water renewal layer.

The volume budget at the two moorings in Douglas Channel does not close under the assumption of uniform cross-channel velocities. In both seasons, at both moorings, there is an up-fjord directed transport equivalent in magnitude to the individual layer transports. We note that the channel is narrow (3–5 km) relative the internal Rossby radius (8 km) so we do not expect substantial cross-channel variations. However, there could be headland eddies and flow separations that make for more complicated cross-channel structure than we expect. In Knight Inlet [*Baker and Pond*, 1995], the net volume transport was estimated to be 1 order of magnitude larger than the mean freshwater input, and cross-channel variation was invoked to explain the imbalance.

In Douglas Channel, there is another potential explanation. As noted by *Webster* [1980b] the head of the fjord system is not the Kitimat River at the head of Douglas Channel but the mouth of the Kitlope River at the head of Gardner Canal. As such, the interpretation of the volume and salt transports in Douglas Channel in terms of an estuarine flow conceptual model requires understanding the partitioning of the freshwater leaving Gardner Canal between the two potential outflow pathways: Verney Passage and Douglas Channel. As discussed by *Webster* [1980b] the partition of the freshwater likely depends on the spatial patterns of both the wind and the recent freshwater inputs as each will affect the pressure gradients along Devastation Channel which connects Gardner Canal, Verney Passage and Douglas Channel. This partitioning was not addressed by the mooring program discussed here and the origin of the volume imbalance observed in Douglas Channel remains an open question.

Douglas Channel is not isolated—it is closely connected to the neighbouring shelf region. In the winter the connection is through the upper inflow layer and in the summer it is thought the deep renewal event. Therefore, changes in the shelf water properties and biota should be expected to appear in Douglas Channel within a season or so. In addition, any changes in the timing of the regional transitions between upwelling and downwelling regimes should be expected to have an immediate impact on the timing of the renewal season.

6.2. Wind-Driven Circulation

The wind-driven response was also investigated. The near-surface current velocity fluctuations and the surface elevation slope are dominated by the along-channel wind. The near-surface currents (4–5 m) at KSK1 and FOC1 are well correlated with the wind (r^2 ranges from 0.43 to 0.56) and the surface current fluctuations were about 2–4% of the wind speed depending on the period of the analysis: the rule of thumb is about 3% [*Weber*, 1983]. From the relationship between the wind and the sea level slope between Kitimat and Hartley Bay, we were able to estimate that the mean direct effect of the wind on the currents extended to 8–12 m into the water column, which is consistent with the vertical profile of the correlation between the wind and the currents. We suspect that the range in value of the coupling term between the wind and surface current is due to differences in the mixing and stratification during the analysis periods. As such the application of the relationship between the wind and the currents to estimate surface drift should respect the uncertainty in the value of the coupling coefficient.

The wind-induced changes in the surface slope in the channel should cause upwelling and downwelling at the head of the channel and result in isopycnal changes. Evidence was found for changes in near-surface (12–14 m) density gradients linked to the surface pressure gradient. We were able to estimate that the baroclinic and barotropic pressure gradients should balance at approximately 30 m. Below that depth we expect the change in the baroclinic term is the one that causes the changes in the velocity profile. We hypothesize that the peak of the anticorrelation between wind and currents at 114 m is a signature of the barotropic response to the wind. These finding are consistent with our results in similar inlets (e.g., enhanced or reversed surface outflow observed in Alberni Inlet, *Farmer and Osborn* [1976], *Farmer* [1976]; Puget Sound, *Matsuura and Cannon* [1997]; Knight Inlet, *Baker and Pond* [1995]; Reloncavi Fjord, *Castillo et al*. [2012], and counter-currents at depth at around 100 m in Puget Sound, *Matsuura and Cannon* [1997]).

The overall circulation in Douglas Channel in the seasonal and meteorological bands is a complex mixture of estuarine flow, directly wind-driven flow, and the barotropic and baroclinic responses to changes to the

surface pressure gradient caused by the wind-driven currents. One unresolved question is "What controls the thickness of the surface fresh layer and the thickness of the surface outflow layer." The analysis with the Wedderburn number indicates that the magnitude of the surface wind plays an important role but wind mixing does not seem to be the entire answer. The role of internal wave mixing from waves generated at the various sills (including the 30 m deep sill in Verney Passage), and from other topographic features has not been addressed here. Not only are the answers to these questions essential in understanding the physical dynamics of the system, but they will also help us make better decisions to support the response planning for various pollutants, which may be neutrally buoyant at various depths in different seasons. The next natural research step would be to implement numerical models to study the subtidal circulation to explore the ideas suggested here. For example, it was clear that the wind mixing and the freshwater discharge alone cannot explain the thickness of the first outflow layer, and numerical "experiments" should provide a better understanding of other mixing mechanisms that could contribute to the first layer formation.

Acknowledgments

Data are available upon request from the corresponding author (diwan@uvic.ca). The authors would like to thank Bodo de Lange Boom at Canadian Hydrographic Service for discussions on the tide gauge data; the officers and crew of the research vessels CCG Tully and CCG Vector for helping us with the mooring deployment and recovery; Tamas Juhasz, David Spear, Lucius Perreault, Andrew Lee, and others at the Institute of Ocean Sciences who helped with the mooring work and initial data processing; Richard Thomson and Jody Klymak for discussions during the earlier stages of this paper; and Patrick Cummins and the two anonymous reviewers for their constructive reviews and suggestions for making it a better paper. This work was supported by Fisheries and Oceans Canada through the World Class Prevention, Preparedness and Response to Oil Spills from Ships Initiative.

References

Arneborg, L., and C. Erlandsson (2004), The rate of inflow and mixing during deep-water renewal in a sill fjord, *Limnol. Oceanogr.*, *49*(3), 768–777, doi:10.4319/lo.2004.49.3.0768.

Baker, P., and S. Pond (1995), The low-frequency residual circulation in Knight Inlet, British Columbia, *J. Phys. Oceanogr.*, *25*, 747–763, doi: 10.1175/1520-0485(1995)025 < 0747:TLFRCI>2.0.CO;2.

Benjamin, T. B. (1968), Gravity currents and related phenomena, *J. Fluid Mech.*, *31*, 209–248.

Castillo, M. I., O. Pizarro, U. Cifuentes, N. Ramirez, and L. Djurfeldt (2012), Subtidal dynamics in a deep fjord of southern Chile, *Cont. Shelf Res.*, *49*, 73–89, doi:10.1016/j.csr.2012.09.007.

Crawford, W. R. (2001), Oceans of the Queen Charlotte Islands, *Can. Tech. Rep. Fish. Aquat. Sci. 2383*, Inst. of Ocean Sci., Sidney, B. C.

de Young, B., and S. Pond (1988), The deepwater exchange cycle in Indian Arm, British Columbia, *Estuarine Coastal Shelf Sci.*, *26*, 285–308, doi:10.1016/0272-7714(88)90066-2.

Farmer, D. M. (1976), The influence of wind on the surface layer of a stratified inlet. Part II: Analysis, *J. Phys. Oceanogr.*, *6*, 941–952, doi: 10.1175/1520-0485(1976)006 < 0941:TIOWOT>2.0.CO;2.

Farmer, D. M., and H. J. Freeland (1983), The physical oceanography of fjords, *Prog. Oceanogr.*, *12*, 147–220, doi:10.1016/0079-6611(83)90004-6.

Farmer, D. M., and T. R. Osborn (1976), The influence of wind on the surface layer of a stratified inlet. Part I: Observations, *J. Phys. Oceanogr.*, *6*, 932–940, doi:10.1175/1520-0485(1976)006 < 0931:TIOWOT>2.0.CO;2.

Farmer, D. M., and D. J. Smith (1980), Tidal interaction of stratified flow with a sill in Knight Inlet, *Deep Sea Res., Part A*, *27*, 239–254, doi: 10.1016/0198-0149(80)90015-1.

Freeland, H. J., and D. M. Farmer (1980), Circulation and energetics of a deep, strongly stratified inlet, *Can. J. Fish. Aquat. Sci.*, *37*, 1398–1410, doi:10.1139/f80-179.

Geyer, W. R. (1997), Influence of wind on dynamics and flushing of shallow estuaries, *Estuarine Coastal Shelf Sci.*, *44*(6), 713–722, doi: 10.1006/ecss.1996.0140.

Geyer, W. R., and G. A. Cannon (1982), Sill processes related to deep water renewal in a fjord, *J. Geophys. Res.*, *87*(C10), 7985–7996, doi: 10.1029/JC087iC10p07985.

Godin, G. (1972), *The Analysis of Tides*, 285 pp., Univ. of Toronto Press, Toronto.

Government of British Columbia (2016), Great bear rainforest (forest management) act, Bill 2. [Available at https://www.leg.bc.ca/parliamentary-business/legislation-debates-proceedings/40th-parliament/5th-session/bills/progress-of-bills.]

Halverson, M. J., C. Bélanger, and S. M. Gay (2013), Seasonal transport variations in the straits connecting Prince William Sound to the Gulf of Alaska, *Cont. Shelf Res.*, *63*, 63–78, doi:10.1016/j.csr.2012.06.017.

Hansen, D. V., and M. Rattray (1966), New dimensions in estuary classification, *Limnol. Oceanogr.*, *XI*, 319–326, doi:10.4319/lo.1966.11.3.0319.

Inall, M. E., F. Nilsen, F. R. Cottier, and R. Daae (2015), Shelf/fjord exchange driven by coastal-trapped waves in the Arctic, *J. Geophys. Res. Oceans*, *120*(12), 8283–8303, doi:10.1002/2015JC011277.

Knudsen, M. (1900), Ein hydrographischer Lehrsatz, *Annu. Hydrogr. Maritimen Meteorol.*, *28*(7), 316–320.

Large, W. G., and S. Pond (1981), Open ocean momentum flux measurements in moderate to strong winds, *J. Phys. Oceanogr.*, *11*, 324–336, doi:10.1175/1520-0485(1981) 011 < 0324:OOMFMI>2.0.CO;2.

LeBlond, P. H., H. Ma, F. Doherty, and S. Pond (1991), Deep and intermediate water replacement in the Strait of Georgia, *Atmos. Ocean*, *29*(2), 288–312, doi:10.1080/07055900.1991.9649406.

Macdonald, R. (1983), Proceedings of a workshop on the Kitimat Marine Environment, *Can. Tech. Rep. Hydrogr. Ocean Sci. 18*, 218 pp., Inst. of Ocean Sci., Dep. of Fish. and Oceans, Patricia Bay, Sidney, B. C.

Macdonald, R., W. J. Cretney, and C. S. Wong (1983), Chemical characteristics of water in the Kitimat fjord system, in *Proceedings of a Workshop on the Kitimat Marine Environment*, *Can. Tech. Rep. of Hydrogr. Ocean Sci. 18*, edited by R. W. Macdonald, pp. 67–88, Inst. of Ocean Sci., Sidney, B. C.

Masson, D. (2002), Deep water renewal in the Strait of Georgia, *Estuarine Coastal Shelf Sci.*, *54*(1), 115–126, doi:10.1006/ecss.2001.0833.

Masson, D., and P. F. Cummins (2007), Temperature trends and interannual variability in the Strait of Georgia, British Columbia, *Cont. Shelf Res.*, *27*(5), 634–649, doi:10.1016/j.csr.2006.10.009.

Matsuura, H., and G. A. Cannon (1997), Wind effects on sub-tidal currents in Puget Sound, *J. Oceanogr.*, *53*(1), 53–66, doi:10.1007/BF02700749.

Morrison, J., M. G. G. Foreman, and D. Masson (2012), A method for estimating monthly freshwater discharge affecting British Columbia Coastal Waters, *Atmos. Ocean*, *50*(1), 1–8, doi:10.1080/07055900.2011.637667.

Pickard, G. (1961), Oceanographic features of inlets in the British Columbia Mainland Coast, *J. Fish. Res. Board Canada*, *18*(6), 907–999, doi: 10.1139/f83-131.

Saarikoski, H., K. Raitio, and J. Barry (2013), Understanding 'successful' conflict resolution: Policy regime changes and new interactive arenas in the Great Bear Rainforest, *Land Use Policy*, *32*, 271–280, doi:10.1016/j.landusepol.2012.10.019.

Stigebrandt, A. (1981), A mechanism governing the estuarine circulation in deep, strongly stratified fjords, *Estuarine Coastal Shelf Sci.*, *13*(2), 197–211, doi:10.1016/S0302-3524(81)80076-X.

Stigebrandt, A. (2012), Hydrodynamics and circulation of fjords, in *Encyclopedia of Lakes and Reservoirs*, edited by R. W. F. Lars Bengtsson and R. W. Herschy, pp. 327–344, Springer, New York, doi:10.1007/978-1-4020-4410-6.

Syvitski, J. P., D. C. Burrell, and J. M. Skei (1987), *Fjords: Processes and Products*, 1st ed., 379 pp., Springer, New York, doi:10.1002/jqs.3390040311.

Thomson, R. E. (1981), Oceanography of the British Columbia Coast, 291 pp., *Can. Spec. Publ. Fish. Aquat. Sci. 56*, Ottawa, Elsevier B. V.

Thomson, R. E., and W. J. Emery (2014), *Data Analysis Methods in Physical Oceanography*, 3rd ed., 728 pp., Newnes, Elsevier B. V.

Weber, J. E. (1983), Steady wind-and wave-induced currents in the open ocean, *J. Phys. Oceanogr.*, *13*, 524–530, doi:10.1175/1520-0485(1983)013 < 0524:SWAWIC>2.0.CO;2.

Webster, I. (1980a), Kitimat Physical Oceanographic Study 1977–1978. Part 1: Data collection and analyses, *Can. Data Rep. Hydrogr. Ocean Sci. 80-3*, Inst. of Ocean Sci., Sidney, B. C.

Webster, I. (1980b), Kitimat Physical Oceanographic Study 1977–1978. Part 3: Estuarine circulation, *Can. Data Rep. Hydrogr. Ocean Sci. 80-3*, Inst. of Ocean Sci., Sidney, B. C.

Wright, C., S. Vagle, C. G. Hannah, and S. Johannessen (2015), Physical, chemical and biological oceanographic data collected in douglas channel and the approaches to Kitimat, June 2013–July 2014, *Can. Data Rep. Hydrogr. Ocean Sci. 196*, iv + 26 pp., Inst. of Ocean Sci., Sidney, B. C.

Wright, C., S. Vagle, C. G. Hannah, S. Johannessen, D. J. Spear, and D. Wan (2016), Physical, chemical and biological oceanographic data collected in Douglas Channel and the approaches to Kitimat, October 2014–July 2015, *Can. Data Rep. Hydrogr. Ocean Sci. 200*, viii + 74 pp., Inst. of Ocean Sci., Sidney, B. C.

Young, C., I. McAllister, and K. McAllister (1997), *The Great Bear Rainforest: Canada's Forgotten Coast*, 144 pp., Harbour Pub., Madeira Park, B. C.